J. Fluid Mech. (2007), *vol.* 584, *pp.* 23–43.
doi:10.1017/S0022112007006234 Printed in the United Kingdom

Streamline topology in the near wake of a circular cylinder at moderate Reynolds numbers

MORTEN BRØNS[1]†, BO JAKOBSEN[1,2], KRISTINE NISS[1,2], ANDERS V. BISGAARD[1]‡ AND LARS K. VOIGT[3]‖

[1]Department of Mathematics, Technical University of Denmark, Building 303S, DK-2800 Kongens Lyngby, Denmark

[2]Department of Mathematics and Physics, Roskilde University, PO Box 260, DK-4000 Roskilde, Denmark

[3]Department of Mechanics, Technical University of Denmark, Building 403, DK-2800 Kongens Lyngby, Denmark

(Received 16 November 2006 and in revised form 25 February 2007)

For the flow around a circular cylinder, the steady flow changes its topology at a Reynolds number around 6 where the flow separates and a symmetric double separation zone is created. At the bifurcation point, the flow topology is locally degenerate, and by a bifurcation analysis we find all possible streamline patterns which can occur as perturbations of this flow. We show that there is no *a priori* topological limitation from further assuming that the flow fulfils the steady Navier–Stokes equations or from assuming that a Hopf bifurcation occurs close to the degenerate flow.

The steady flow around a circular cylinder experiences a Hopf bifurcation for a Reynolds number about 45–49. Assuming that this Reynolds number is so close to the value where the steady separation occurs that the flow here can be considered a perturbation of the degenerate flow, the topological bifurcation diagram will contain all possible instantaneous streamline patterns in the periodic regime right after the Hopf bifurcation. On the basis of the spatial and temporal symmetry associated with the circular cylinder and the structure of the topological bifurcation diagram, two periodic scenarios of instantaneous streamline patterns are conjectured. We confirm numerically the existence of these scenarios, and find that the first scenario exists only in a narrow range after the Hopf bifurcation whereas the second one persists through the entire range of Re where the flow can be considered two-dimensional. Our results corroborate previous experimental and computational results.

1. Introduction

The prototype configuration for the study of the flow around a bluff body is the circular cylinder. A huge body of theoretical, experimental and computational results exists, and yet it is still a research field of considerable contemporary interest. The basic features of the flow are well-known (Williamson 1996; Coutanceau & Defaye 1991). For low Reynolds numbers $Re = UD/\nu$, where U is the velocity of the incoming

† Author to whom correspondence should be addressed: m.brons@mat.dtu.dk.
‡ Present address: NKT Flexibles I/S, Priorparken 510, DK-2605 Brøndby, Denmark.
‖ Present address: ANSYS Europe Ltd, West Central 127, Milton Park, Abingdon, Oxfordshire, OX14 4SA, UK.

flow, D is the cylinder diameter, and ν is the kinematic viscosity of the fluid, the flow is two-dimensional and attached to the cylinder. The flow field has mirror-symmetry with respect to the streamwise direction. For $Re = Re_S \approx 5$–7, the flow separates and two counter-rotating steady vortices are created behind the cylinder, such that the symmetry of the flow is preserved. At $Re = Re_H \approx 45$–49, the steady flow becomes unstable, and a regime with a periodic flow follows. In this regime, vortices are shed periodically from the cylinder, resulting in the von Kármán vortex street. For higher values of Re, the flow becomes three-dimensional and turbulent.

The change of streamline pattern at Re_S is not associated with a hydrodynamic instability (Noack & Eckelmann 1994*b*). For all Re below Re_H, there is a unique steady stable solution to the Navier–Stokes equations. It is only the topology of the streamlines of the steady velocity field which changes at Re_S. In contrast, several computational and experimental studies have established that the change to periodic flow at Re_H is due to a supercritical Hopf bifurcation (Jackson 1987; Provansal, Mathis & Boyer 1987; Zebib 1987; Dŭsek, Le Gal & Fraunié 1994; Noack & Eckelmann 1994*a*). In the Hopf bifurcation, the symmetric steady velocity field loses stability to a periodically varying field which does not possess the mirror symmetry of the steady flow, and hence introduces new topologies of the instantaneous streamline patterns.

Changes in the topology of streamlines as described above can be studied systematically with the aid of the theory of dynamical systems. For a time-dependent velocity field $\boldsymbol{v}(\boldsymbol{x}, t)$, the equations for the instantaneous streamlines at $t = t_0$ are

$$\frac{\mathrm{d}\boldsymbol{x}}{\mathrm{d}t} = \boldsymbol{v}(\boldsymbol{x}, t_0). \tag{1}$$

Applying bifurcation theory to this system of ordinary differential equations of dimension two or three, we can obtain an overview of possible changes in flow topology (Perry & Chong 1987; Bakker 1991; Brøns 2007). This approach has been used to analyse a variety of specific steady flows, for example the flow in a driven cavity (Gürcan & Deliceoğlu 2005), slip-flows (Tophøj, Møller & Brøns 2006), and vortex breakdown (Brøns, Voigt & Sørensen 1999; Brøns & Bisgaard 2006). Our purpose here is to perform a topological analysis of the possible flow patterns close to the body in the wake of a circular cylinder, extending previously similar analyses of steady flows to include periodic flows.

A bifurcation analysis of a streamline pattern is initiated by locating a degenerate flow which marks the transition between regimes with different flow topologies. For the flow around a cylinder, we take this to be the flow at Re_S where the steady vortices are created. We then obtain an *unfolding* of this flow pattern, that is, a parameterized family of flow fields in which the topology of all possible perturbations of the degenerate field is represented. With the aid of normal form theory we obtain this unfolding assuming only that the flow is incompressible and fulfils the no-slip boundary condition on the cylinder wall. The analysis generalizes that of Bakker (1991) who assumed that the body was flat and the flow was steady. We show, however, that neither of these assumptions limit the possible flow topologies.

We find the bifurcation diagram for the unfolding which yields a complete catalogue of possible streamline patterns which can occur as perturbations of the degenerate flow. Possible perturbations include a distortion of the body shape and a variation of Re.

If we assume that changing Re from around Re_S to around Re_H is such a perturbation, then all possible streamline patterns in the periodic regime just after the Hopf bifurcation will be represented in the unfolding.

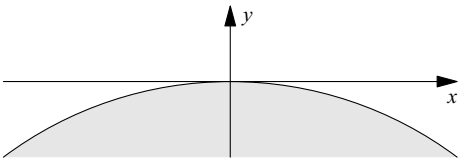

FIGURE 1. The coordinate system near a no-slip wall.

We analyse whether the extra conditions on the flow arising from the Hopf bifurcation in the Navier–Stokes equations give any further restrictions on the flow topology, and find this not to be the case. Hence, all streamline topologies represented in the unfolding can, in principle, occur as instantaneous streamline patterns in the periodic flow after the Hopf bifurcation. From the structure of the bifurcation diagram, we find that one particular scenario, that is, a sequence of instantaneous streamline patterns, must occur right after the bifurcation. As the amplitude of the periodic oscillations grows as Re is increased away from Re_H, further bifurcation curves may be crossed, and new streamline topologies appear. From the relative size of the different regions in the bifurcation diagram, one such scenario is argued to be the most likely to occur.

We confirm these qualitative predictions by numerical simulations. We find that the first scenario only occurs in a very narrow range after the Hopf bifurcation, and that the second proposed scenario then exists for Re up to 200.

The first systematic study of instantaneous streamlines in the wake of a circular cylinder was undertaken by Perry, Chong & Lim (1982). They performed an extensive analysis of experimental streamline patterns in the wake of a cylinder, leading to a conjecture for the sequence of the instantaneous streamline patterns in the periodic regime. Eaton (1987) verified numerically the part of the proposed patterns which are closest to the cylinder, but also showed that the sequence was incomplete. Some further patterns were found which live only for a relatively short time, and hence escaped the attention of Perry *et al.* (1982).

The second scenario we find is identical to that of Eaton (1987). Hence, in addition to providing a general analysis of possible streamline patterns close to almost-circular bodies in the steady and periodic regime, we specifically obtain a theoretical clarification of the results by Perry *et al.* (1982) and Eaton (1987).

The paper is organized as follows. In § 2, we derive the normal form for the unfolding of the degenerate flow pattern and analyse its bifurcation structure. In § 3, we discuss the influence of the Navier–Stokes equations on the streamline topology, and numerical results are given in § 4. Conclusions are drawn in § 5.

2. Local streamline patterns and their bifurcations

2.1. *The normal form*

In this section we consider the local streamline pattern close to a no-slip wall of arbitrary shape. We consider the flow close to a given point which we take to be the origin in an (x, y) coordinate system (figure 1). The coordinate system is attached tangentially to the wall, its surface being locally described by $y = f(x)$, where f has the power series expansion

$$f(x) = \sum_{n=2}^{\infty} b_n x^n. \tag{2}$$

For the flow around a circular cylinder, the origin will be the aft point of symmetry.

Assuming that the flow is incompressible, a streamfunction ψ exists such that the velocity components are given by

$$u = \frac{\partial \psi}{\partial y}, \quad v = -\frac{\partial \psi}{\partial x}. \tag{3}$$

We assume that ψ has a power series expansion

$$\psi(x, y) = \sum_{n,m=0}^{\infty} \psi_{n,m} x^n y^m. \tag{4}$$

We will perform a number of coordinate changes to simplify ψ. The first transformation is

$$r = x, \quad s = y - f(x), \tag{5}$$

which takes the wall $y = f(x)$ to the r-axis. One easily finds that the no-slip condition $\partial\psi/\partial r = \partial\psi/\partial s = 0$ at $s = 0$ yields that s^2 is a factor of ψ. Hence, it has an expansion of the form

$$\psi(r, s) = s^2 \tilde{\psi} = s^2 \sum_{n,m=0}^{\infty} a_{n,m+2} r^n s^m. \tag{6}$$

The relations between the original $\psi_{n,m}$, the expansion coefficients b_n for the wall shape, and the transformed $a_{n,m}$ are easily found from (5).

The streamlines are the trajectories of the ordinary differential equations

$$\dot{r} = \frac{\partial \psi}{\partial s} = 2s\tilde{\psi} + s^2 \frac{\partial \tilde{\psi}}{\partial s}, \quad \dot{s} = -\frac{\partial \psi}{\partial r} = -s^2 \frac{\partial \tilde{\psi}}{\partial r}. \tag{7}$$

The equations have a common factor s, and, in accordance with the no-slip condition, all points on the wall are critical. Dividing by the common factor, corresponding to scaling the time by a factor s, yields the equivalent system

$$\dot{r} = 2\tilde{\psi} + s \frac{\partial \tilde{\psi}}{\partial s}, \quad \dot{s} = -s \frac{\partial \tilde{\psi}}{\partial r}. \tag{8}$$

Writing the lowest-order terms explicitly, we find

$$\begin{pmatrix} \dot{r} \\ \dot{s} \end{pmatrix} = \begin{pmatrix} 2a_{0,2} \\ 0 \end{pmatrix} + \begin{pmatrix} 2a_{1,2} & 3a_{0,3} \\ 0 & -a_{1,2} \end{pmatrix} \begin{pmatrix} r \\ s \end{pmatrix} + O(2). \tag{9}$$

If $a_{0,2} = 0$, the origin is a critical point. If $a_{1,2} \neq 0$, it is a hyperbolic saddle, which is either a point of separation or attachment. If $a_{1,2} = 0$, the critical point is degenerate, and higher-order terms determine the local behaviour of the streamlines. We consider now the degenerate case $a_{1,2} = 0$ when furthermore the flow field is compatible with the symmetry of the flow around a circular cylinder. For the mirror-symmetric flow we have

$$u(-r, s) = -u(r, s), \quad v(-r, s) = v(r, s). \tag{10}$$

This is fulfilled when all terms in (6) with an even power of r are zero,

$$a_{2n,m} = 0 \quad (n, m = 0, 1, 2, \ldots). \tag{11}$$

It will follow from the analysis (and is shown with the method of the blowing up of a singularity by Bakker 1991) that to resolve the degeneracy, terms up to the fifth order must be included in ψ. Hence, we consider now the streamfunction (6) with the conditions (11),

$$\psi = \psi_0 = a_{1,3} r s^3 + a_{3,2} r^3 s^2 + a_{1,4} r s^4 + O(6). \tag{12}$$

We will assume the non-degeneracy conditions

$$a_{3,2} \neq 0, \quad a_{1,4} \neq 0. \tag{13}$$

To simplify ψ, we use an almost-linear transformation defined by

$$r = \alpha_{1,0}\xi + \alpha_{0,1}\eta + \alpha_{2,0}\xi^2 + \alpha_{1,1}\xi\eta + \alpha_{0,2}\eta^2, \tag{14a}$$

$$s = \eta + \beta_{1,1}\xi\eta + \beta_{0,2}\eta^2. \tag{14b}$$

The factor η in (14*b*) ensures that the wall $s=0$ is mapped to the line $\eta=0$. The inverse transformation is well-defined close to the origin as long as $\alpha_{1,0} \neq 0$, but otherwise the coefficients can be chosen freely.

Inserting the transformation (14) into (12) yields an expression of the form

$$\psi = \bar{a}_{1,3}\xi\eta^3 + \bar{a}_{0,4}\eta^4 + \bar{a}_{2,3}\xi^2\eta^3 + \bar{a}_{3,2}\xi^3\eta^2 + \bar{a}_{1,4}\xi\eta^4 + \bar{a}_{0,5}\eta^5 + O(6). \tag{15}$$

Terms which were not present in (12) have been introduced by the transformation. They have the coefficients

$$\bar{a}_{0,4} = a_{1,3}\alpha_{0,1}, \tag{16a}$$

$$\bar{a}_{2,3} = 3\beta_{1,1}a_{1,3}\alpha_{1,0} + 3a_{3,2}\alpha_{0,1}{\alpha_{1,0}}^2 + a_{1,3}\alpha_{2,0}, \tag{16b}$$

$$\bar{a}_{0,5} = a_{1,3}\alpha_{0,2} + a_{3,2}{\alpha_{0,1}}^3 + 3\beta_{0,2}a_{1,3}\alpha_{0,1} + a_{1,4}\alpha_{0,1}. \tag{16c}$$

These terms can be removed again by choosing

$$\alpha_{0,1} = \alpha_{0,2} = 0, \quad \alpha_{2,0} = -3\beta_{1,1}\alpha_{1,0}. \tag{17}$$

With this, the remaining coefficients are

$$\bar{a}_{1,3} = a_{1,3}\alpha_{1,0}, \quad \bar{a}_{3,2} = a_{3,2}\alpha_{1,0}^3, \quad \bar{a}_{1,4} = a_{1,3}(\alpha_{1,1} + 3\alpha_{1,0}\beta_{0,2}) + a_{1,4}\alpha_{1,0}. \tag{18}$$

By choosing

$$\alpha_{1,1} = 0, \quad \beta_{0,2} = -\frac{a_{1,4}}{3a_{1,3}}, \tag{19}$$

$\bar{a}_{1,4}$ vanishes. No further terms can be removed, but $\bar{a}_{1,3}$ and $\bar{a}_{3,2}$ can be made to have the same absolute value if

$$\alpha_{1,0} = \sqrt{|a_{1,3}/a_{3,2}|}. \tag{20}$$

The last undetermined coefficient in the transformation is $\beta_{1,1}$. As it does not appear in the transformed ψ, we set it to zero. The resulting streamfunction is

$$\psi_0 = a_{1,3}\sqrt{\left|\frac{a_{1,3}}{a_{3,2}}\right|}\xi\eta^2(\eta + \sigma\xi^2) + O(6), \tag{21}$$

where

$$\sigma = \left|\frac{a_{1,3}}{a_{3,2}}\right|\frac{a_{3,2}}{a_{1,3}} = \pm 1. \tag{22}$$

The truncated normal form from (21) which is obtained by dropping the O-term is easily analysed. The streamlines through the origin are $\xi=0, \eta=0$ and $\eta=-\sigma\xi^2$. Depending on σ, there are either three or one separatrices going into the fluid from the critical point (figure 2).

We are, however, not interested only in the flow topology at the exact degeneracy. We also want to consider the situation where the streamfunction is close to that, and will include the general terms missing in (12) as perturbation terms. Hence, we consider the streamfunction

$$\begin{aligned}\psi = s^2(&\epsilon_{2,0} + \epsilon_{1,2}r + \epsilon_{0,3}s + \epsilon_{2,2}r^2 + a_{1,3}rs \\ &+ \epsilon_{0,4}s^2 + a_{3,2}r^3 + \epsilon_{2,3}r^2s + a_{1,4}rs^2 + \epsilon_{0,5}s^3 + O(4))\end{aligned} \tag{23}$$

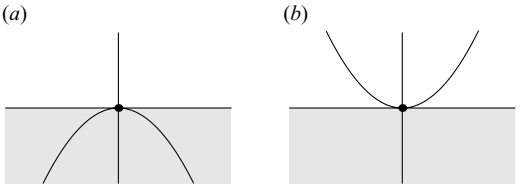

FIGURE 2. Topology of the degenerate critical point. (*a*) $\sigma = +1$. (*b*) $\sigma = -1$. The shaded region is below the wall.

We collect the 7 small parameters in a vector $\boldsymbol{\epsilon} = (\epsilon_{2,0}, \epsilon_{1,2}, \epsilon_{0,3}, \epsilon_{2,2}, \epsilon_{0,4}, \epsilon_{2,3}, \epsilon_{0,5})^T$. We use again the transformation (14) to simplify ψ as much as possible. We add a constant term $\alpha_{0,0}$ in the definition of r to allow a translation of the coordinate system along the wall. Inserting, and making a Taylor expansion yields an expression of the form

$$\begin{aligned}\psi = \eta^2(&\overline{a}_{2,0} + \overline{a}_{1,2}\xi + \overline{a}_{0,3}\eta + \overline{a}_{2,2}\xi^2 + \overline{a}_{1,3}\xi\eta + \overline{a}_{0,4}\eta^2 \\ &+ \overline{a}_{3,2}\xi^3 + \overline{a}_{2,3}\xi^2\eta + \overline{a}_{1,4}\xi\eta^2 + \overline{a}_{0,5}\eta^3 + O(4)).\end{aligned} \tag{24}$$

Each of the $\overline{a}_{n,m}$ depend on the original expansion parameters $a_{k,l}$, the perturbation parameters $\boldsymbol{\epsilon}$, and the 8 parameters in the transformation,

$$\boldsymbol{\lambda} = (\alpha_{0,0}, \alpha_{1,0}, \alpha_{0,1}, \alpha_{2,0}, \alpha_{1,1}, \alpha_{0,2}, \beta_{1,1}, \beta_{0,2})^T. \tag{25}$$

Define the nine-dimensional vector function

$$\boldsymbol{F}(\boldsymbol{\lambda}, \boldsymbol{\epsilon}) = (\overline{a}_{0,2}, \overline{a}_{1,2}, \overline{a}_{0,3}, \overline{a}_{2,2}, \overline{a}_{0,4}, \overline{a}_{2,3}, \overline{a}_{0,5}, \overline{a}_{1,4}, \overline{a}_{3,2} - \sigma\overline{a}_{1,3})^T. \tag{26}$$

With

$$\boldsymbol{\lambda}_0 = (0, \sqrt{|a_{1,3}/a_{3,2}|}, 0, 0, 0, 0, 0, -a_{1,4}/(3a_{1,3}))^T \tag{27}$$

we have $\boldsymbol{F}(\boldsymbol{\lambda}_0, \boldsymbol{0}) = \boldsymbol{0}$, corresponding to the transformation in the degenerate case. If we could extend this to a general solution $\boldsymbol{\lambda} = \boldsymbol{\lambda}(\boldsymbol{\epsilon})$ with $\boldsymbol{\lambda}(\boldsymbol{0}) = \boldsymbol{\lambda}_0$ such that $\boldsymbol{F}(\boldsymbol{\lambda}(\boldsymbol{\epsilon}), \boldsymbol{\epsilon}) = \boldsymbol{0}$ for $|\boldsymbol{\epsilon}|$ small, we would have obtained the normal form (21) independent of $\boldsymbol{\epsilon}$. This is, however, not possible. The 9×8 Jacobian matrix $D_{\boldsymbol{\lambda}}\boldsymbol{F}(\boldsymbol{\lambda}_0, \boldsymbol{0})$ has rank 6, indicating that only six parameters influence the value of $\boldsymbol{F}$ and only six of the equations in $\boldsymbol{F} = \boldsymbol{0}$ can be fulfilled. Inspired by the degenerate case where α_{11} and $\beta_{1,1}$ were of no importance, we choose them to be zero, and consider a reduced parameter vector of dimension 6,

$$\boldsymbol{\mu} = (\alpha_{0,0}, \alpha_{1,0}, \alpha_{0,1}, \alpha_{2,0}, \alpha_{0,2}, \beta_{0,2})^T, \tag{28}$$

and a reduced function of dimension 6,

$$\boldsymbol{G}(\boldsymbol{\mu}, \boldsymbol{\epsilon}) = (\overline{a}_{2,2}, \overline{a}_{0,4}, \overline{a}_{2,3}, \overline{a}_{0,5}, \overline{a}_{1,4}, \overline{a}_{3,2} - \sigma\overline{a}_{1,3})^T, \tag{29}$$

obtained by dropping the first three components of $\boldsymbol{F}$, corresponding to retaining only conditions on the highest-order terms of ψ. We find

$$\boldsymbol{G}(\boldsymbol{\mu}_0, \boldsymbol{0}) = \boldsymbol{0}, \quad \det D_{\boldsymbol{\mu}}\boldsymbol{G}(\boldsymbol{\mu}_0, \boldsymbol{0}) = 18a_{3,2}^2 a_{1,3}^4 \left|\frac{a_{1,3}}{a_{3,2}}\right|^{5/2} \neq 0. \tag{30}$$

It follows from the implicit function theorem that there exists a vector function $\boldsymbol{\mu}(\boldsymbol{\epsilon})$, $\boldsymbol{\mu}(\boldsymbol{0}) = \boldsymbol{\mu}_0$, such that $\boldsymbol{G}(\boldsymbol{\mu}(\boldsymbol{\epsilon}), \boldsymbol{\epsilon}) = \boldsymbol{0}$ for $|\boldsymbol{\epsilon}|$ small, as desired. Finally, dividing by $\overline{a}_{1,3}$, corresponding to scaling the time with that factor, the streamfunction becomes

$$\psi = \eta^2(c_{0,2} + c_{1,2}\xi + c_{0,3}\eta + \xi\eta + \sigma\xi^3 + O(4)), \tag{31}$$

with three transformed small parameters,

$$c_{0,2} = \frac{\overline{a}_{0,2}}{\overline{a}_{1,3}} = \sqrt{\left|\frac{a_{3,2}}{a_{1,3}}\right|}\frac{\epsilon_{0,2}}{a_{1,3}} + O(|\boldsymbol{\epsilon}|^2), \tag{32a}$$

$$c_{1,2} = \frac{\overline{a}_{1,2}}{\overline{a}_{1,3}} = \frac{\epsilon_{1,2}}{a_{1,3}} + O(|\boldsymbol{\epsilon}|^2), \tag{32b}$$

$$c_{0,3} = \frac{\overline{a}_{0,3}}{\overline{a}_{1,3}} = -\sqrt{\left|\frac{a_{3,2}}{a_{1,3}}\right|}\left(\frac{2a_{1,4}\epsilon_{0,2}}{3a_{1,3}^2} - \frac{\epsilon_{0,3}}{a_{1,3}} + \frac{\epsilon_{2,2}}{3a_{3,2}}\right) + O(|\boldsymbol{\epsilon}|^2). \tag{32c}$$

The latter identities are obtained from a first-order Taylor expansion of $\boldsymbol{\mu}(\boldsymbol{\epsilon})$ by implicit differentiation.

The normal form transformation has reduced the number of small parameters from seven to three, and we can obtain all possible local flow topologies which can appear as perturbations of the degenerate configuration from (31). It constitutes the desired unfolding of the degenerate flow at $\boldsymbol{\epsilon} = \mathbf{0}$. Of the original small parameters, only four appear linearly in (32). We can pick out a subset of three from this list, e.g. $\epsilon_{0,2}, \epsilon_{1,2}, \epsilon_{0,3}$, which can be considered as key parameters in the following sense. For a given small value of the three $c_{n,m}$ and the remaining four $\epsilon_{n,m}$, it is possible to choose $\epsilon_{0,2}, \epsilon_{1,2}, \epsilon_{0,3}$ such that (32) is fulfilled. This follows from the implicit function theorem, since the Jacobian matrix

$$\frac{\partial(c_{0,2}, c_{1,2}, c_{0,3})}{\partial(\epsilon_{0,2}, \epsilon_{1,2}, \epsilon_{0,3})} \tag{33}$$

is regular for $\boldsymbol{\epsilon} = \mathbf{0}$. That is, by varying the three key parameters only, independent of the remaining $\epsilon_{n,m}$, the full unfolding (31) can be attained. We will use this in § 3.

2.2. *Bifurcation analysis of the normal form*

Here, we analyse the bifurcation structure of the truncated normal form for $\sigma = +1$,

$$\psi = y^2(c_{0,2} + c_{1,2}x + c_{0,3}y + xy + x^3), \tag{34}$$

where, for simplicity, we have renamed the coordinates back to x, y.

Before we embark on a complete analysis of (34), it is instructive to consider the case which fulfils the symmetry conditions (11), that is $c_{0,2} = c_{0,3} = 0$,

$$\psi = xy^2(c_{1,2} + y + x^2). \tag{35}$$

The differential equations for the streamlines (8) become

$$\dot{x} = \hat{u} = 2c_{1,2}x + 3xy + 2x^3, \quad \dot{y} = \hat{v} = -y(c_{1,2} + y + 3x^2). \tag{36}$$

The critical points on the wall $y = 0$ satisfy $\hat{u} = 0$, that is

$$c_{1,2}x + x^3 = 0. \tag{37}$$

This has solutions $x = 0$ and $x = \pm\sqrt{-c_{1,2}}$. The latter exist only for $c_{1,2} < 0$. The off-wall critical points satisfy $\hat{v}/y = 0$, that is

$$y = -c_{1,2} - 3x^2. \tag{38}$$

Inserting (38) into $\hat{u} = 0$ yields

$$-c_{1,2}x - 7x^3 = 0, \tag{39}$$

with solutions $x = 0$ and $x = \pm\sqrt{-c_{1,2}/7}$. Again, the latter exist only for $c_{1,2} < 0$, and, as they have $y = -4c_{1,2}/7$, they are above the wall for all $c_{1,2} < 0$.

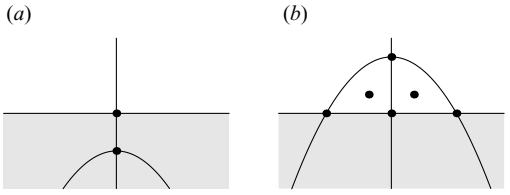

FIGURE 3. Bifurcation in the symmetric normal form (35). (*a*) $c_{1,2} > 0$. (*b*) $c_{1,2} < 0$.

The bifurcation is summarized in figure 3. We see that decreasing $c_{1,2}$ through zero corresponds to the change of topology which occurs behind the circular cylinder at $Re \approx 5$.

For the general normal form (34), we have to deal with a three-dimensional parameter space $(c_{0,2}, c_{0,3}, c_{1,2})$. The subsequent analysis will show that bifurcations related to streamline patterns above the wall only occur for $c_{1,2} < 0$. The transformation $y \to -y, \sigma \to -\sigma$ gives rise to the change of sign $\psi \to -\psi$. Hence, the streamline patterns below the wall for $\sigma = -1$ are the streamline patterns above the wall for $\sigma = +1$. An analysis of the patterns for $\sigma = -1$ is performed by Niss & Jakobsen (2003).

Equations (8) become

$$\dot{x} = \hat{u} = 2c_{0,2} + 2c_{1,2}x + 3c_{0,3}y + 3xy + 2x^3, \quad \dot{y} = \hat{v} = -y(c_{1,2} + y + 3x^2). \tag{40}$$

We note, that the system is invariant under the symmetry

$$c_{0,2} \to -c_{0,2}, \quad c_{0,3} \to -c_{0,3}, \quad x \to -x. \tag{41}$$

Critical points on the wall $y = 0$ satisfy

$$\hat{u} = 2c_{0,2} + 2c_{1,2}x + 2x^3 = 0. \tag{42}$$

Up to three critical points can exist, and bifurcation occurs when the number of solutions changes. This happens when the discriminant of (42) is zero,

$$-4c_{1,2}^3 - 27c_{0,2}^2 = 0, \tag{43}$$

or

$$c_{0,2} = \pm 2\sqrt{-\frac{c_{1,2}^3}{27}}. \tag{44}$$

In figure 4, these are the curves marked I and I'. Crossing these curves, a recirculating zone attached to the wall is created or destroyed.

Critical points off the wall satisfy $\hat{v}/y = -(c_{1,2} + y + 3x^2) = 0$, from which

$$y = -c_{1,2} - 3x^2, \tag{45}$$

$$\hat{u} = 2c_{0,2} - 3c_{0,3}c_{1,2} - c_{1,2}x - 9c_{0,3}x^2 - 7x^3 = 0. \tag{46}$$

Again, up to three critical points can exist, and the number of solutions changes when the discriminant is zero,

$$1323c_{0,2}^2 - 1458c_{0,3}^3c_{0,2} - 3402c_{0,2}c_{1,2}c_{0,3} + 7c_{1,2}^3 + 2187c_{0,3}^4c_{1,2} + 2106c_{1,2}^2c_{0,3}^2 = 0. \tag{47}$$

This is a quadratic equation in $c_{0,2}$ with two solutions, each describing a curve in the $c_{0,3}, c_{0,2}$ parameter plane for fixed $c_{1,2}$. They are marked II and II' in figure 4. Crossing these curves, a saddle and a centre are created or destroyed. The curve II

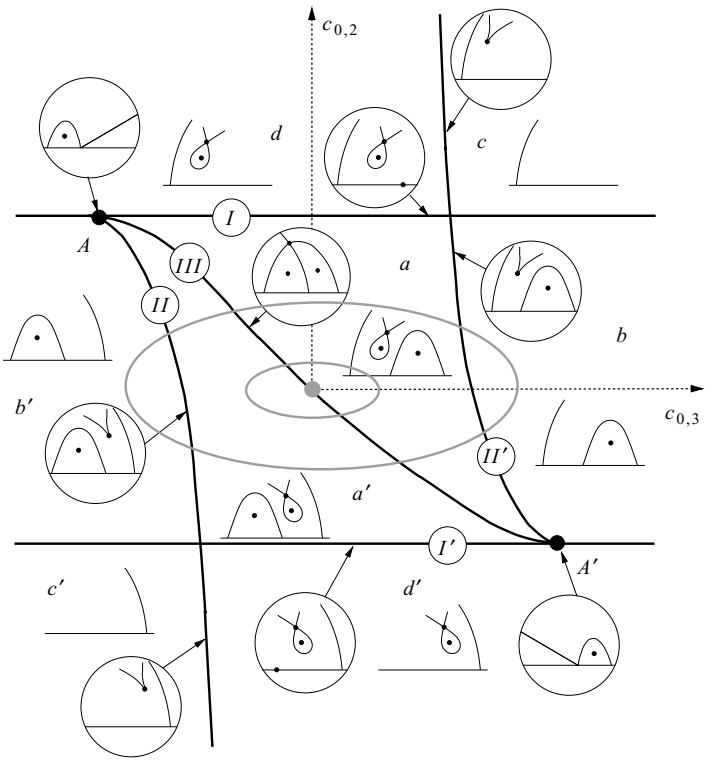

FIGURE 4. A slice in the bifurcation diagram for the normal form (34) in the $\boldsymbol{c} = (c_{0,2}, c_{0,3}, c_{1,2})$ parameter space for a negative value of $c_{1,2}$. For clarity, the diagram is not to scale. The grey marker and the two grey ellipses indicate the steady separated flow and the two periodic scenarios, respectively, for the flow around a circular cylinder discussed in § 3.

touches I tangentially at

$$A : (c_{0,3}, c_{0,2}) = \left(-\tfrac{1}{3}\sqrt{-3c_{1,2}},\, \tfrac{2}{9}(-3c_{1,2})^{3/2}\right). \tag{48}$$

Although the curve defined by (47) extends beyond A, it does not define a bifurcation here, as the bifurcating critical points are below the surface.

At A, a degenerate critical point on the wall with a zero Jacobian exists, but without the symmetry (10). The unfolding of this degeneracy was found by Hartnack (1999). The analysis shows that in addition to the bifurcation curves I and II, there is also a curve of global bifurcations emanating from A, corresponding to a flow topology where the separatrices of the off-wall saddle point are connected to the on-wall critical points. Such a configuration occurs when $\psi = 0$ at the off-wall saddle point, given by (45), (46). From this, we find that the bifurcation curve, marked by III in figure 4, is given by

$$c_{0,2} = c_{0,3}\left(c_{1,2} - c_{0,3}^2\right). \tag{49}$$

Again, only the part corresponding to the critical point being above the wall is of interest. The local structure of the bifurcation diagram near A is mirrored close to $A' = -A$, where I' and II' meet tangentially. The global bifurcation curve emanating from A' is identical to III.

This concludes the bifurcation analysis from which we have obtained a partition of the $\boldsymbol{c} = (c_{0,2}, c_{0,3}, c_{1,2})$ parameter space for $c_{1,2} < 0$ into open sets $a - d$ with regular

streamline topologies and bifurcation sets *I–III* with degenerate flow patterns together with their mirror images in $a' - d'$ and $I', II', III' = III$. For $c_{1,2} > 0$, no bifurcations occur, and only the topology c (which is the same as c') occurs.

3. The topological role of the Navier–Stokes equations

Until now, we have assumed only that the flow is incompressible and satisfies the no-slip boundary condition at the wall. However, the Navier–Stokes equations must also be fulfilled, and we now address whether this gives rise to limitations in the bifurcations found in § 2.2.

We first consider the role of the steady Navier–Stokes equations. We write these in vorticity form,

$$(\boldsymbol{v}\cdot\nabla)\omega - \frac{1}{Re}\Delta\omega = 0, \tag{50}$$

where $\boldsymbol{v} = (u, v)$ and vorticity ω is

$$\omega = \frac{\partial u}{\partial y} - \frac{\partial v}{\partial x} = \Delta\psi. \tag{51}$$

Taking the expansion (6) of the streamfunction and transforming it back to Cartesian coordinates (x, y) using (5) and inserting into (50) yields

$$\begin{aligned}
&\frac{8}{Re}\left(3b_2^2\epsilon_{0,2} + \epsilon_{2,2} + b_2\epsilon_{0,3} + 3\epsilon_{0,4}\right)\\
&\quad + \frac{24}{Re}\left(10b_2b_3\epsilon_{0,2} - 5b_2^2\epsilon_{1,2} + a_{3,2} - 3a_{1,3}b_2 - 3b_3\epsilon_{0,3} + a_{1,4}\right)x\\
&\quad + \left(-4\epsilon_{0,2}\epsilon_{1,2} + \frac{24}{Re}\left(-2b_4\epsilon_{0,2} + 3b_2^2\epsilon_{0,3}y - 2b_2\epsilon_{2,2} - 2b_3\epsilon_{1,2} - 4b_2\epsilon_{0,4} + \epsilon_{2,3} + 5\epsilon_{0,5}\right)\right)y\\
&\quad + \cdots = 0.
\end{aligned} \tag{52}$$

In (52) we have, as before, renamed those $a_{n,m}$ which are small when the flow is close to degenerate to $\epsilon_{n,m}$. There is no need to keep track of terms of higher order in the power series, as they will introduce terms of order six and higher from ψ. These terms do not influence the topology of the streamlines, as the unfolding (31), which is of order five, gives a complete qualitative description of the flow.

We get three equations from setting the coefficients in (52) equal to zero. These can be solved for three parameters as functions of the others in various way. For example,

$$\epsilon_{2,2} = -3\left(b_2^2\epsilon_{0,2} - b_2\epsilon_{0,3} + \epsilon_{0,4}\right), \tag{53a}$$

$$\epsilon_{0,5} = \frac{1}{5}\left(\frac{Re}{6}\epsilon_{0,2}\epsilon_{1,2} + 2b_4\epsilon_{0,2} + 3b_2^2\epsilon_{0,3} - 6b_2^3\epsilon_{0,2} - 2b_2\epsilon_{0,4} + 2b_3\epsilon_{1,2} - \epsilon_{2,3}\right), \tag{53b}$$

$$a_{1,4} = -10b_2b_3\epsilon_{0,2} - 5b_2^2\epsilon_{1,2} - a_{3,2} + 3a_{1,3}b_2 + 3b_3\epsilon_{0,3}. \tag{53c}$$

Equations (53) reduce the number of free perturbation parameters by two from the original seven. However, the set of key parameters discussed at the end of § 2.1 is not affected, and hence no limitation in the free variation of $c_{0,2}$, $c_{1,2}$, $c_{0,3}$ is imposed. Furthermore, as the normal form transformation removes the term $a_{1,4}rs^4$ from ψ, the value of $a_{1,4}$ is of no importance and (53*c*) has no topological information. Hence, we conclude that the steady Navier–Stokes equations do not give rise to any topological limitations. All streamline topologies and bifurcations occurring in the normal form (31) may be realized in steady flows.

We now turn to the role of the Hopf bifurcation. Consider a family of steady flows parameterized by Re. Denote the streamfunction at some given Re_0 by ψ_0 with a corresponding velocity field $\boldsymbol{v}_0$ and vorticity ω_0. A small perturbation field given by $\psi_1, \boldsymbol{v}_1, \omega_1$ fulfils the linearized Navier–Stokes equations

$$\frac{\partial \omega_1}{\partial t} + (\boldsymbol{v}_0 \cdot \nabla)\omega_1 + (\boldsymbol{v}_1 \cdot \nabla)\omega_0 = \frac{1}{Re_0}\Delta\omega_1 \tag{54}$$

as well as the no-slip boundary conditions. The parameter value Re_0 is a Hopf bifurcation point if (54) has a harmonic solution of the form $\psi_1 = \tilde{B}(x, y)\,\mathrm{e}^{\mathrm{i}\beta t}$. The periodic solution appearing close to the Hopf bifurcation is

$$\psi \approx \psi_0(x, y) + \delta(\tilde{B}(x, y)\,\mathrm{e}^{\mathrm{i}\beta t} + \tilde{B}(x, y)^*\,\mathrm{e}^{-\mathrm{i}\beta t}), \tag{55}$$

where the asterisk denotes complex conjugation and $\delta \approx \sqrt{Re - Re_0}$ (Wiggins 1990).

We now consider the following expansions of the streamfunctions,

$$\psi_0 = s^2 \sum_{n,m=0}^{\infty} A_{n,m+2} r^n s^m, \tag{56}$$

$$\psi_1 = \left(s^2 \sum_{n,m=0}^{\infty} B_{n,m+2} r^n s^m \right) \mathrm{e}^{\mathrm{i}\beta t}, \tag{57}$$

and if the Taylor expansion of the periodic solution is denoted

$$\psi = s^2 \sum_{n,m=0}^{\infty} a_{n,m+2} r^n s^m, \tag{58}$$

it follows from (55) that

$$a_{n,m} \approx A_{n,m} + \delta(B_{n,m}\,\mathrm{e}^{\mathrm{i}\beta t} + B^*_{n,m}\,\mathrm{e}^{-\mathrm{i}\beta t}). \tag{59}$$

Further, inserting this into (32) yields that a periodic solution is represented by a closed curve in the $\boldsymbol{c}$ parameter space, encircling the point representing the steady solution. We have already seen that a steady solution close to the degeneracy may occur as any point in the $\boldsymbol{c}$-space. The question is now whether the conditions from the linearized Navier–Stokes equations yield any topological constraints on the way the periodic solution can be embedded in the parameter space. To this end, we transform (56) and (57) back to the original variables (x, y) and insert into (54) to obtain

$$\begin{aligned}
&2\beta B_{0,2}\,\mathrm{i} - 8\frac{3b_2^2 B_{0,2} + B_{2,2} - 3b_2 B_{0,3} + 3B_{0,4}}{Re_0} \\
&\quad + \left(2\beta B_{1,2}\,\mathrm{i} - 24\frac{10b_2 b_3 B_{0,2} + 5b_2^2 B_{1,2} + B_{3,2} - 3b_2 B_{1,3} - 3b_3 B_{0,3} + B_{1,4}}{Re_0} \right) x \\
&\quad + \Bigg(4(A_{1,2}B_{0,2} + A_{0,2}B_{1,2}) + 2(3B_{0,3} - 2b_2 B_{0,2})\beta i \\
&\quad - 24\frac{-2b_4 B_{0,2} + 3b_2^2 B_{0,3} - 2b_2 B_{2,2} - 2b_3 B_{1,2} - 4b_2 B_{0,4} + B_{2,3} + 5B_{0,5}}{Re_0} \Bigg) y \\
&\quad + \ldots = 0.
\end{aligned} \tag{60}$$

We can solve the three equations arising from setting the coefficients in the power series equal to zero. We choose to solve for the same coefficients as in the steady case,

and find

$$B_{2,2} = \frac{\mathrm{i}\beta Re_0}{4} B_{0,2} - 3B_{0,2}b_2^2 + 3B_{0,3}b_2 - 3B_{0,4}, \tag{61a}$$

$$B_{0,5} = \frac{1}{5}\left[\mathrm{i}\beta Re_0\left(\tfrac{1}{3}B_{0,2}b_2 + \tfrac{1}{4}B_{0,3}\right) + \frac{Re_0}{6}(A_{1,2}B_{0,2} + A_{0,2}B_{1,2}) + 2B_{0,2}b_4 + 3B_{0,3}b_2^2 - 6B_{0,2}b_2^3 - 2B_{0,4}b_2 + 2B_{1,2}b_3 - B_{2,3}\right], \tag{61b}$$

$$B_{1,4} = \frac{\mathrm{i}\beta Re_0}{12} B_{1,2} - 10B_{0,2}b_2b_3 - 5B_{1,2}b_2^2 - B_{3,2} + 3B_{1,3}b_2 + 3B_{0,3}b_3. \tag{61c}$$

Again, these do not provide any bounds on the set of key parameters. It follows that *a priori* the periodic solution may have any sequence of instantaneous streamline topology represented in the bifurcation diagram in figure 4.

However, for the flow around a circular cylinder, the fact that the periodic solution grows smoothly out of the steady solution combined with the symmetry properties does give us some directions about which flow topologies to expect. The steady symmetric separated solution has $c_{0,2} = c_{0,3} = 0$ and only $c_{1,2}$ varies with Re. This flow is represented in figure 4 as the origin. Furthermore, the periodic solutions have a temporal symmetry, as

$$u(x, y, t + T/2) = -u(-x, y, t), \quad v(x, y, t + T/2) = v(-x, y, t), \tag{62}$$

where T is the period. This expresses that the second half-period of the flow is the mirror image of the first half-period. This symmetry follows from the symmetry of the boundary conditions and because there is a unique family of periodic solutions to the Navier–Stokes equations in the range we consider here. As a consequence, a periodic solution is represented by a symmetric closed curve in the bifurcation diagram in figure 4.

Thus, directly after the Hopf bifurcation, the periodic solution must be represented by a small symmetric closed curve encircling the origin in the bifurcation diagram. Such a solution is represented by the small grey ellipse in figure 4. Hence, the instantaneous streamline pattern must switch between a and a' at each half-period when the bifurcation curve *III* is crossed.

When Re increases, the amplitude of the periodic flow increases, and the corresponding closed curve in the bifurcation diagram also grows. From the topological analysis alone, we cannot infer the way this happens. However, from figure 5, it appears that in the $\boldsymbol{c}$ parameter space, the region with the topologies a and a' is very narrow. From this, one would expect that the closed curve will soon cross the curves *II* and *II*′ and also attain the topologies b and b' during a period. As the bifurcation lines *I* and *I*′ are relatively far away, it seems unlikely that these curves are reached before that. Hence, the most probable next scenario is indicated as the large grey ellipse in figure 4. In § 4, we will verify this sequence of events numerically.

4. Numerical results

Numerical simulations are performed in dimensionless variables based on the cylinder diameter D and a time scale D/U, where U is the incoming flow velocity. We use the finite volume code developed by Michelsen (1992) and Sørensen (1995). The code solves the two-dimensional laminar Navier–Stokes equations in Cartesian coordinates. Because of the convective nature of the flow, the SUDS difference scheme is employed to ensure a stable solution for the steady-state simulations, whereas the less diffusive central difference scheme is employed for the unsteady simulations. For

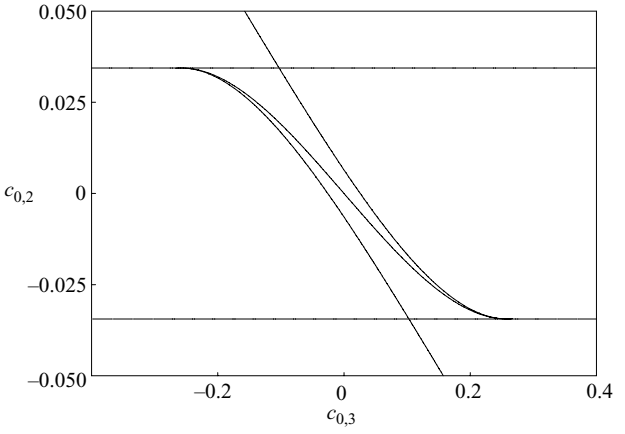

FIGURE 5. The bifurcation diagram from figure 4 to scale for $c_{1,2} = 0.1$, showing the relative size of the different regions with different streamline topologies.

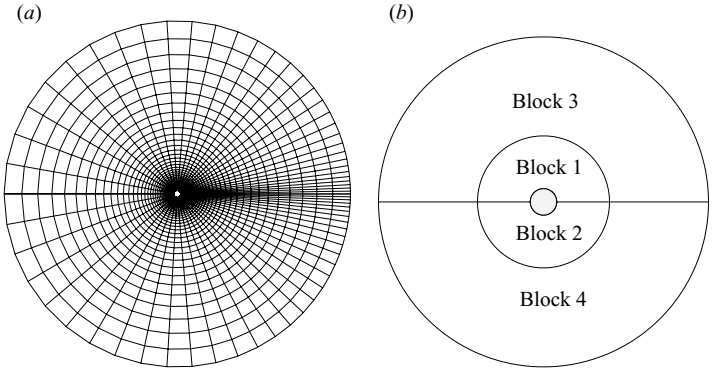

FIGURE 6. The structure of the computational grid. (*a*) A 32×32 grid. For clarity, the grid shown is coarser than the standard 64×64 grid used in simulations. (*b*) The block structure.

the pressure–velocity coupling, the SIMPLE algorithm is used for the steady-state simulation. For the unsteady simulations, the PISO algorithm with an additional corrector step was used. A preliminary study of the streamline topology using the code was performed by Petersen (2002).

In this section we use an x, y coordinate system with origin at the centre of the cylinder with x being in the streamwise direction. The computational grid is defined in the corresponding polar coordinates r, θ. The grid is of annular shape with outer diameter $50D$. This was found to be sufficient to ensure that the development of the flow structures in the wake of the cylinder is not influenced by boundary conditions. The computations are performed on structured multiblock grids with four blocks. In each block, a polar grid of size $N \times N$ with grid points (r_i, θ_j) is used. To ensure a high density of grid points near the cylinder and in the wake, the distances between the radial grid points are chosen with a uniform growth rate, $r_{i+1} - r_i = B(r_i - r_{i-1})$, with $B = 1.0495$. The angular grid points are chosen with a non-uniform growth rate which is minimal at $\theta = 0$. An example of the grid and block structure is shown in figure 6. In the standard net, each block consists of 64×64 cells, but for validation purposes, sample computations are also performed on a finer grid with 128×128 cells.

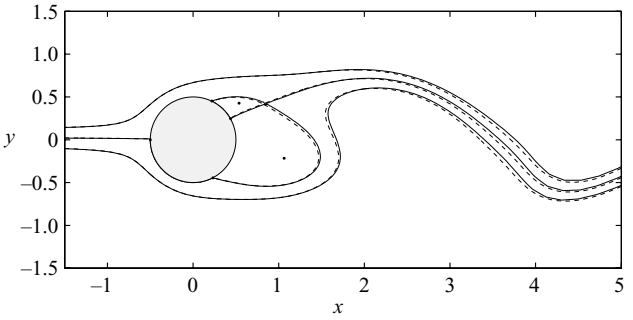

FIGURE 7. Comparison of streamlines obtained with the standard grid (full lines) and the fine grid (dashed lines) for $Re = 100$ at a time instant where the bifurcation line *III* is crossed.

Critical point	Normal grid		Fine grid		Relative error
	x	y	x	y	(%)
Upper vortex centre	0.537	−0.428	0.520	0.427	2.48
Lower vortex centre	1.063	−0.216	1.022	−0.215	3.78
Upper separation point	0.219	0.452	0.221	0.452	0.40
Middle separation point	0.438	0.248	0.436	0.250	0.56
Lower separation point	0.232	−0.446	0.229	−0.445	0.63
In-flow saddle point	0.842	0.413	0.814	0.413	2.99

TABLE 1. A comparison of the critical points found at the normal and the fine grid. The relative error is defined as $\|\boldsymbol{x}_{\text{normal}} - \boldsymbol{x}_{\text{fine}}\| / \|\boldsymbol{x}_{\text{normal}}\|$.

On the cylinder wall, no-slip boundary conditions are fulfilled. On the outer boundary, a constant velocity $(u, v) = (1, 0)$ is imposed. In the unsteady simulations, we have used a time step $\mathrm{d}t = 0.0025$, which is sufficiently small to ensure a stable transient solution.

In figure 7, we compare the streamlines for the standard and fine grids for $Re = 100$ for the periodic solution at a time instant where a closed separation bubble exists, i.e. at the bifurcation line *III* in figure 4. Only representative streamlines, in particular the dividing streamlines and the critical points, are shown. The in-flow critical points are located by computing the isoclines, that is, the curves where $u = 0$ and $v = 0$ and finding their points of intersection. The dividing streamlines are consequently found by plotting the iso-curves of ψ corresponding to the value of ψ attained at the saddle point, and the on-wall points of separation are then given as the points where these iso-curves meet the cylinder.

We see that there is very good agreement between the two simulations, in particular in the region of interest close to the cylinder. This is confirmed quantitatively in table 1 where the positions of the critical points are compared. It appears that the in-flow critical points are more sensitive to the grid size than the on-wall separation points. This is probably due to the relatively simple method used to locate these points. Nevertheless, we find that for the present qualitative study, an error of below 5 % is acceptable.

Furthermore, we have computed the dimensionless frequency, the Strouhal number $St = fd/U$, in the periodic regime (figure 8). We compare with the relation of the

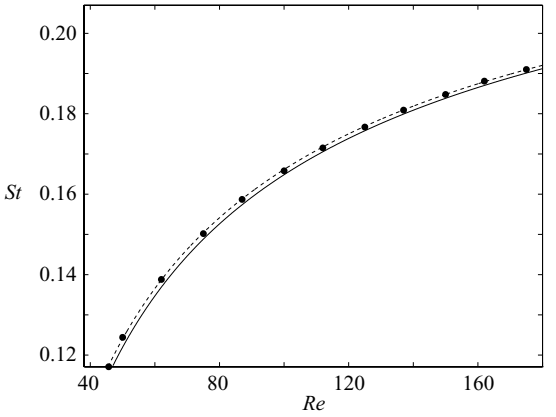

FIGURE 8. Strouhal number *St vs. Re* in the periodic regime. The markers indicate numerical simulations, and a fit to the data of the form (63) is shown as the dashed line. The full line is the relation (63) obtained by Fey *et al.* (1998).

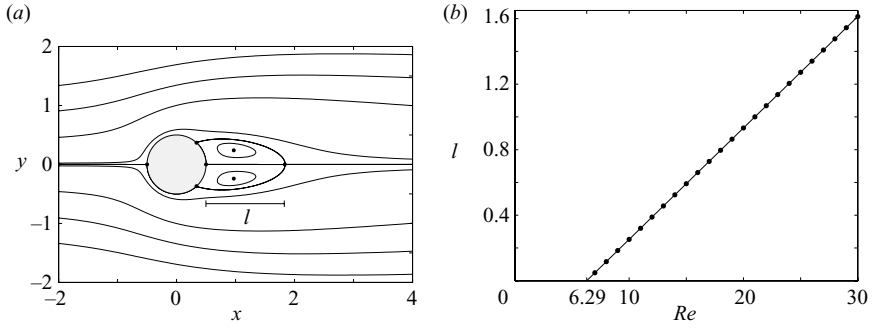

FIGURE 9. (*a*) Streamlines for $Re = 26$, in the steady separated regime, shown in dimensionless coordinates based on cylinder diameter D. The separation bubble length l is indicated. (*b*) Dimensionless bubble length l as a function of Re. The markers show results from simulations, the line is the linear fit (64) of the data.

form

$$St = A - \frac{B}{\sqrt{Re}} \tag{63}$$

proposed by Fey, König & Eckelmann (1998) on the basis of experiments. Fey *et al.* obtain $A = 0.2684$, $B = 1.0356$. By fitting our data to the functional form (63), we obtain $A = 0.2678$, $B = 1.0168$.

We conclude that the normal grid is sufficient to resolve the streamline topology, and it will be used from now on.

Our first aim is to locate the topological bifurcation point Re_S where the two steady vortices behind the cylinder are created. To this end, we have measured the length of the recirculation zone (figure 9*a*) for various $Re > Re_S$. A linear trend is clearly seen in figure 9(*b*). A least-squares fit gives

$$l = 0.068Re - 0.428, \tag{64}$$

from which we obtain $Re_S = 6.29$. This is in good agreement with other results from the literature. Zielinska *et al.* (1997) find numerically $l = 0.0670(\pm 0.0008)Re - 0.405(\pm 0.035)$, which yields $Re_S = 6.0 \pm 0.5$. Dennis & Chang (1970) find numerically

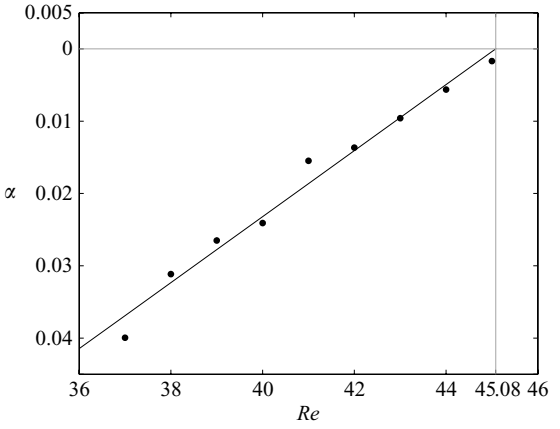

FIGURE 10. Growth rate α as a function of Re for the velocity component v in the point $(x, y) = (7.42, 0.48)$. The markers show the results from fitting the time series to the expression (65), and the line is a linear fit to the markers.

Re_S between 5 and 7, whereas Noack & Eckelmann (1994*b*) find $Re_S = 5 \pm 1$ with a low-dimensional Galerkin method. Experimentally, Taneda (1956) finds that the separation occurs for some Re between 6 and 7.

To locate the Hopf bifurcation, we follow Hernández & Pacheco (2002). In the steady regime, we perform dynamic simulations and consider the development of the transient. Eventually, only the slowest decaying mode will be present, and when Re is close to Re_H it will be characterized by a complex eigenvalue $\lambda = \alpha + \mathrm{i}\beta$, $\alpha < 0$. Thus, a velocity component (we choose v) in a fixed point in the fluid will asymptotically have the form

$$v = v_0 + c\mathrm{e}^{\alpha t} \sin(\beta t + \phi), \tag{65}$$

for $t \to \infty$. Fitting the time series for v with the expression (65), the growth rate α can be estimated. Figure 10 shows the growth rate as a function of Re for a downstream point in the fluid. Extrapolating the linear fit to $\alpha = 0$ yields that the Hopf bifurcation occurs at $Re = 45.08$. We have repeated the procedure for a point inside the separated region, $(x, y) = (2.09, -0.01)$, and obtain here the bifurcation point $Re = 45.22$. We will take the average of the two values as the Hopf bifurcation point, $Re_H = 45.15$. This is slightly lower than the experimental value $Re = 49$ (Williamson 1996) and the value $Re = 47.1$ obtained computationally by Dŭsek *et al.* (1994).

For $Re = 45.6$, directly after the Hopf bifurcation, the flow is periodic with a period $T = 8.57$, corresponding to 3428 time steps. During the period, we see the instantaneous streamline topologies as shown in figure 11. Fixing the phase such that the bifurcation curve *III* is crossed at $t = 0$, we find the topology a' for $t \in]0, T/2[$. For $t = T/2$, *III* is crossed again, and the topology a follows for $t \in]T/2, T[$. This corresponds to traversing the small grey ellipse in figure 4 counterclockwise.

Increasing Re to 100, the period decreases to $T = 6.03$ (2412 time steps), and a different scenario occurs (figure 12). As conjectured in § 3, the increase of amplitude with Re has introduced the topologies b and b' by crossing the bifurcation curves *II* and *II*′, corresponding to the large grey ellipse in figure 4. As shown in table 2, most of the time is spent in the regions a, a'.

As Re is decreased from 100, the time T_b spent in topology b (or b') decreases, and becomes zero as the scenario changes to the first sequence at some Re_T. To

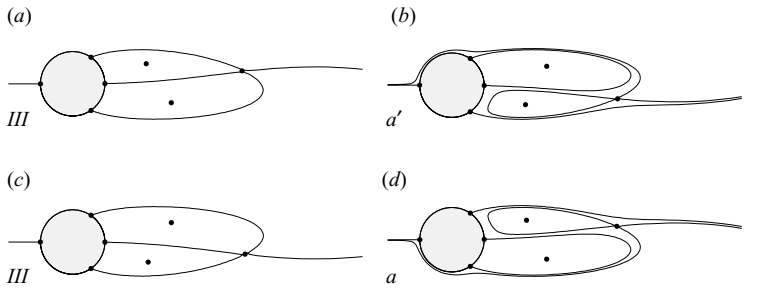

FIGURE 11. The sequence of instantaneous streamlines for $Re = 45.6$. (*a*) $t = 0$, topology *III*. (*b*) Typical streamline pattern for $t \in]0, T/2[$. (*c*) $t = T/2$, topology *III*. (*d*) Typical streamline pattern for $t \in]T/2, T[$.

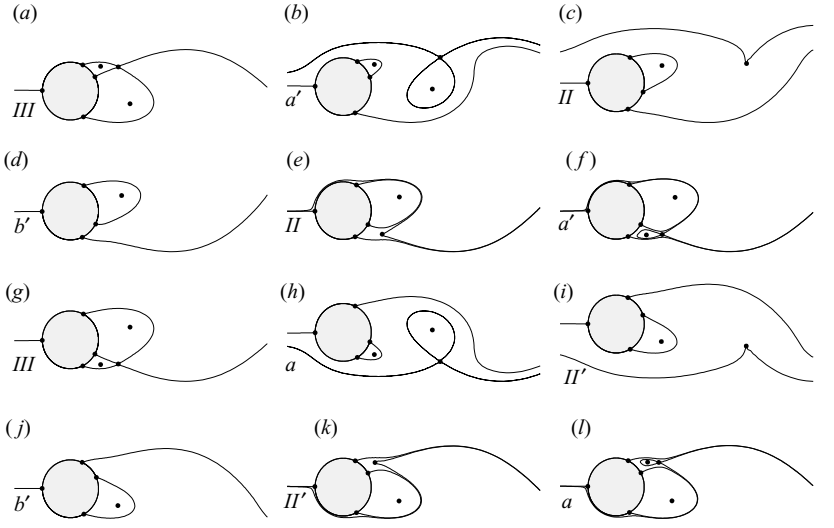

FIGURE 12. The sequence of instantaneous streamlines for $Re = 100$. The patterns at a bifurcation (a, c, e, g, i, k) occur at the phases shown in table 2. The remaining panels show typical patterns of the streamlines within the time interval, they occur between bifurcations.

estimate Re_T we consider the scaling of T_b as $Re \to Re_T$. The distance between the two points where the periodic solution crosses bifurcation curve *II* in the bifurcation diagram scales as $\sqrt{Re - Re_T}$, as the part of the orbit which is in region *b* is locally a parabola. Asymptotically, the speed along this part is constant, and hence T_b also scales as $\sqrt{Re - Re_T}$. In figure 13, T_b^2 is mapped against Re, which, according to the above, should give rise to a linear relationship. This is indeed the case, and extrapolating a linear fit to $T_b^2 = 0$ yields $Re_T = 45.68$. This is very close to the Hopf bifurcation point $Re_H = 45.08$.

The second periodic scenario persists for $Re_T < Re < 200$. We have found some minor further changes in the streamline patterns very close to the cylinder for $Re > 200$, see Bisgaard (2005) for further details. However, as these occur in a regime where the flow has become three-dimensional, the physical relevance is limited, and we will not pursue this further here.

In the scenario proposed by Perry *et al.* (1982), two types of bifurcation occurs. The first is shown in figure 14(*c*). The lower on-wall critical point of the attached

Topology		Phase at bifurcation	Fraction of period spent in region
III		0.0000	
	a'		0.0858
II		0.0858	
	b'		0.0261
II		0.1119	
	a'		0.3881
III		0.5000	
	a		0.0858
II'		0.5858	
	b		0.0261
II'		0.6119	
	a		0.3881
III		1.0000	

TABLE 2. Timing of the topologies during a period at $Re = 100$. The phase is defined in units of the dimensionless period $T = 6.03$ and is chosen to be zero when topology *III* occurs.

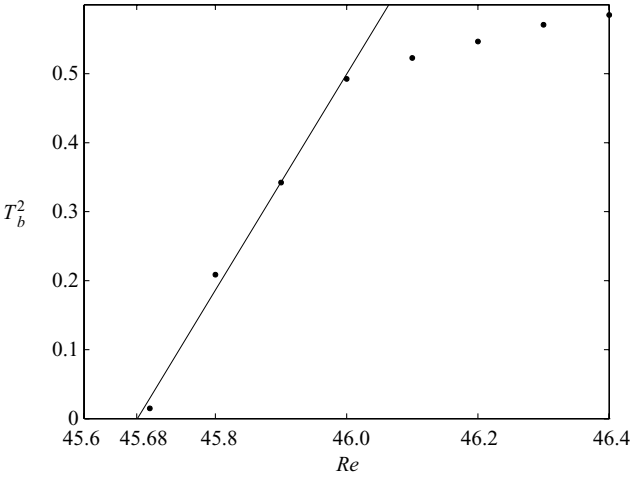

FIGURE 13. Square of time T_b spent at topology b as a function of Re in the second periodic scenario. The markers are data from the simulation, the line is a linear fit of the last four data points. The start of the second periodic scenario is found as $Re_T = 45.68$.

separation zone is assumed to move toward the on-wall critical point with a free separatrix as the zone grows in size. At some time instant, the two critical points merge and form a degenerate critical point, which then disappears and forms an off-wall saddle point. This off-wall structure is then advected downstream. In the second bifurcation (figure 14*d*), a degenerate critical point is created on the cylinder which gives rise to a small attached recirculation zone. The streamline pattern is now the mirror image of the pattern before the first bifurcation, and in the second half of the period the same bifurcations occur again.

This bifurcation scenario is completely legitimate. Hartnack (1999) has shown that this is, in fact, the simplest one that can occur close to a no-slip wall if an attached separation zone and a free separatrix are interacting. This does not, however, take the

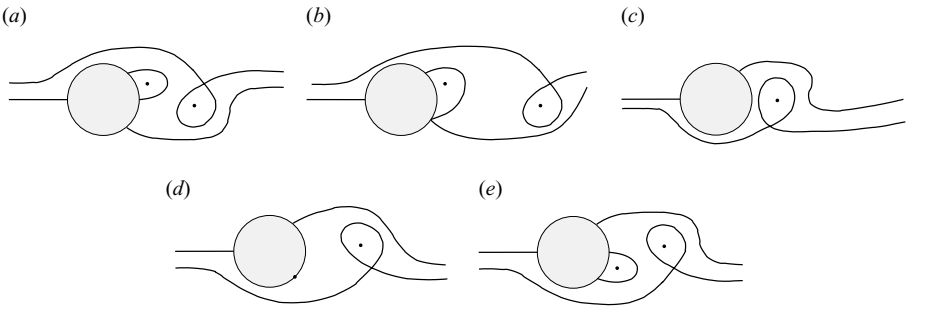

FIGURE 14. The periodic scenario proposed by Perry *et al.* (1982). Only half a period is shown. The upper off-wall saddle loop in (a, b) persists and moves downstream, and is not shown in $(c–e)$ for clarity.

symmetry of the problem into account. The present analysis shows that the topology of the steady separated flow (type *III*) must occur in the sequence of streamline patterns. Hence, the sequence in figure 14 is not to be expected in flows around symmetric or almost symmetric bodies, but may well occur in other cases.

As the scenario by Perry *et al.* (1982) does not include any off-wall bifurcation, the saddle-loops are assumed to persist as they drift downstream. Eaton (1987) found numerically that this does not happen, as they disappear in a bifurcation that we denote *II* and *II*′. Thus, he found the topologies b, b' and further showed that b is transformed into a, *III* and a' during the periodic cycle, in agreement with the present analysis.

5. Conclusions

Two basic bifurcation phenomena occur in the flow around a circular cylinder: the creation of a symmetric recirculation zone at Re_S and a Hopf bifurcation leading to periodic flow at Re_H. We have examined the instantaneous streamline topology in the low-Re regime from the assumption that the two bifurcations are close to each other. From this it follows that the instantaneous streamline patterns which can occur in the periodic regime can all be found in the topological bifurcation diagram which unfolds the degenerate flow at Re_S. This diagram has a simple symmetric structure with few different streamline patterns and it has a high degree of robustness. First, the detailed shape of the solid body is of no importance, as long as its surface is smooth. By coordinate transformations, the body can be transformed to a flat wall, and the shape of the wall represented by the coefficients b_n in (2) plays no role in the qualitative analysis. Secondly, no limitations are imposed from assuming that the flow is steady. This is in contrast to the simpler degeneracy near A and A' in figure 4. For this, there is also a normal form with a sign parameter σ. The bifurcation occurring here is the case of $\sigma = +1$. Hartnack (1999) shows that $\sigma = -1$ is not possible in a steady flow. No similar limitation occurs for the normal form (34). Finally, the assumption that a periodic flow represented by a closed curve in the diagram is created in a Hopf bifurcation imposes no topological constraints.

From the structure of the bifurcation diagram and the symmetry properties of the flow around a circular cylinder, we were able to conjecture the presence of two scenarios for the instantaneous streamlines in the periodic regime and to confirm them numerically. The first scenario exists in an exceedingly small range of Re which is clearly beyond realistic experimental verification. Nevertheless, the existence of this

regime is unavoidable. The only way the structurally unstable topology *III* of the symmetric steady separated flow can bifurcate, is to break the heteroclinic connection between the off-wall and on-wall saddle points, creating either the topology *a* or *a′*. It is not possible to have a smooth transition from the topology *III* directly into the second periodic scenario.

The analysis has implications beyond the flow around a circular cylinder. For other bodies which obey the same mirror-symmetry with respect to the main flow, the same two scenarios in the periodic regime will be expected. For such bodies, the first periodic scenario may exist in a larger range of Re than found here, and the periodic solutions may go farther out in the bifurcation diagram and include further topologies in the regions c, c', d, d' in figure 4. The topological analysis can give no *a priori* information about this; it can only line up possible (and impossible) flow topologies. For bodies which break the mirror symmetry, the steady flow will not be bound to be at the line of symmetry $c_{0,2} = c_{0,3} = 0$, but may be anywhere in the bifurcation diagram. Indeed, Dennis & Young (2003) find numerically the topologies *a* and *b* in the steady flow around ellipses inclined to the free flow. For asymmetric bodies in the periodic regime the solutions may cross the bifurcation lines in various complicated manners, as the symmetry conditions (62) will not be satisfied.

The theory of the present paper is derived from perturbation theory and hence has its limitations. It is spatially local as it is based on a Taylor expansion in the coordinates with the rear point of symmetry of the body as the expansion point. Hence, it cannot account for flow features far away from this point. Furthermore, the normal form can only account for body shapes which are close to symmetric and for Re which are close to the value Re_S where a degenerate flow pattern occur. In particular, to account for the flow topology in the periodic domain, the flow at the Hopf bifurcation point Re_H must be a perturbation of the flow at Re_S. To rigorously determine what is required for a specific flow configuration to be a perturbation of the degenerate symmetric flow, and hence for the present theory to be valid, would require some kind of error estimate which we have not obtained. Nevertheless, the robustness of the theory alluded to above, and the fact that the numerical results of the present paper are in complete agreement with the general theory, indicate a large domain of validity. We may consider the bifurcation diagram in figure 4 as a *topological phase space* for the streamlines close to a large class of bluff bodies in the steady and periodic regimes.

REFERENCES

Bakker, P. G. 1991 *Bifurcations in Flow Patterns*. Kluwer, Dordrecht.

Bisgaard, A. V. 2005 Structures and bifurcations in fluid flows with applications to vortex breakdown and wakes. PhD thesis, Department of Mathematics, Technical University of Denmark.

Brøns, M. 2007 Streamline topology – Patterns in fluid flows and their bifurcations. *Adv. Appl. Mech.* **41**, 1–43.

Brøns, M., Voigt, L. K. & Sørensen, J. N. 1999 Streamline topology of steady axisymmetric vortex breakdown in a cylinder with co- and counter-rotating end-covers. *J. Fluid Mech.* **401**, 275–292.

Brøns, M. & Bisgaard, A. V. 2006 Bifurcation of vortex breakdown patterns in a circular cylinder with two rotating covers. *J. Fluid Mech.* **568**, 329–349.

Coutanceau, M. & Defaye, J.-R. 1991 Circular cylinder wake configurations: flow visualisation survey. *Appl. Mech. Rev.* **44**, 255–305.

Dennis, S. C. R. & Chang, G.-Z. 1970 Numerical solutions for steady flow past a circular cylinder at Reynolds numbers up to 100. *J. Fluid Mech.* **42**, 379–399.

Dennis, S. C. R. & Young, P. J. S. 2003 Steady flow past an elliptic cylinder inclined to the stream. *J. Engng Maths* **47**, 101–120.

Dŭsek, J., Le Gal, P. & Fraunié, P. 1994 A numerical and theoretical study of the first Hopf bifurcation in a cylinder wake. *J. Fluid Mech.* **264**, 59–80.

Eaton, B. E. 1987 Analysis of laminar vortex shedding behind a circular cylinder by computer-aided flow visualization. *J. Fluid Mech.* **180**, 117–145.

Fey, U., König, M. & Eckelmann, H. 1998 A new Strouhal–Reynolds-number relationship for the circular cylinder in the range $47 < Re < 2 \times 10^5$. *Phys. Fluids* **10**, 779–794.

Gürcan, F. & Deliceoğlu, A. 2005 Streamline topologies near nonsimple degenerate points in two-dimensional flows with double symmetry away from boundaries and an application. *Phys. Fluids* **17**, 093106.

Hartnack, J. N. 1999 Streamline topologies near a fixed wall using normal forms. *Acta Mech.* **136** (1–2), 55–75.

Hernández, R. H. & Pacheco, A. 2002 Numerical simulation and experiments of a control method to suppress the Bénard–von Kármán instability. *Eur. Phys. J.* B **30**, 265–274.

Jackson, C. P. 1987 A finite-element study of the onset of vortex shedding in flow past variously shaped bodies. *J. Fluid Mech.* **182**, 23–45.

Michelsen, J. A. 1992 Basis3D – a platform for development of multiblock PDE solvers. AFM 92-05. Department of Fluid Mechanics, Technical University of Denmark.

Niss, K. & Jakobsen, B. 2003 Hopf bifurcation and topology in fluid flow (in Danish). Text no. 412. Department of Mathematics and Physics, Roskilde University.

Noack, B. R. & Eckelmann, H. 1994*a* A global stability analysis of the steady and periodic cylinder wake. *J. Fluid Mech.* **270**, 297–330.

Noack, B. R. & Eckelmann, H. 1994*b* A low-dimensional Galerkin method for the three-dimensional flow around a circular cylinder. *Phys. Fluids* **6**, 124–143.

Perry, A. E. & Chong, M. S. 1987 A description of eddying motions and flow patterns using critical-point concepts. *Annu. Rev. Fluid Mech.* **19**, 125–155.

Perry, A. E., Chong, M. S. & Lim, T. T. 1982 The vortex-shedding process behind two-dimensional bluff bodies. *J. Fluid Mech.* **116**, 77–90.

Petersen, R. 2002 Dynamical systems and structures in the flow around a cylinder. Master's thesis, Department of Mathematics, Technical University of Denmark.

Provansal, M., Mathis, C. & Boyer, L. 1987 Bénard–von Kármán instability: transient and forced regimes. *J. Fluid Mech.* **182**, 1–22.

Sørensen, N. N. 1995 General-purpose flow solver applied over hills. RISØ-R-827-(EN). Risø National Laboartory.

Taneda, S. 1956 Experimental investigation of the wakes behind cylinders and plates at low Reynolds numbers. *J. Phys. Soc. Japan* **11**, 347–384.

Tophøj, L., Møller, S. & Brøns, M. 2006 Streamline patterns and their bifurcations near a wall with Navier slip boundary conditions. *Phys. Fluids* **18**, 083102.

Wiggins, S. 1990 *Introduction to Applied Nonlinear Dynamical Systems and Chaos*. Springer.

Williamson, C. H. K. 1996 Vortex dynamics in the cylinder wake. *Annu. Rev. Fluid Mech.* **28**, 477–539.

Zebib, A. 1987 Stability of viscous flow past a circular cylinder. *J. Engng Maths* **21**, 155–165.

Zielinska, B. J. A., Goujon-Durand, S., Dušek, J. & Wesfreid, J. E. 1997 Strongly nonlinear effect in unstable wakes. *Phys. Rev. Lett.* **79**, 3893–3896.